Observation of a Picosecond Light-Induced Spin Transition in Polymeric Nanorods

Marco Reinhard, Kristjan Kunnus, Kathryn Ledbetter, Elisa Biasin, Diana Bregenholt Zederkof, Roberto Alonso-Mori, Tim Brandt van Driel, Silke Nelson, Michael Kozina, Olaf J. Borkiewicz, et al.

Observation of a picosecond light-induced spin transition in polymeric nanorods

Marco Reinhard[1*], Kristjan Kunnus[1], Kathryn Ledbetter[2^], Elisa Biasin[1#], Diana Bregenholt Zederkof[3&], Roberto Alonso-Mori[1], Tim Brandt van Driel[1], Silke Nelson[1], Michael Kozina[1], Olaf J. Borkiewicz[4], Maciej Lorenc[5], Marco Cammarata[5], Eric Collet[5], Dimosthenis Sokaras[1], Amy A. Cordones[1], Kelly J. Gaffney[1*]

[1]SLAC National Accelerator Laboratory, Menlo Park, California 94025, USA

[2]Department of Physics, Stanford University, Stanford, California 94305, USA

[3]Department of Physics, Technical University of Denmark, 2800 Kongens Lyngby, Denmark

[4]X-ray Science Division, Argonne National Laboratory, Lemont, IL 60439

[5]Univ Rennes, CNRS, IPR (Institut de Physique de Rennes) – UMR 6251, 35000 Rennes, France

Present addresses:

[^]Department of Physics, Harvard University, Cambridge, MA 02138, USA

[#]Physical Sciences Division, Pacific Northwest National Laboratory, Richland, Washington 99352, USA

[&]European XFEL GmbH, Holzkoppel 4, 22869 Schenefeld, Germany

[*]Corresponding authors:

E-mail: marcor@slac.stanford.edu, kgaffney@slac.stanford.edu

Abstract

Spin transition materials are attractive for developing photo-switchable devices but their slow material transformations limit device applications. Size reduction could enable faster switching, but the photoinduced dynamics at the nanoscale remains poorly understood. Here, we report a femtosecond optical pump multimodal X-ray probe study of polymeric nanorods. Simultaneously tracking the spin transition order parameter with X-ray emission spectroscopy and structure with X-ray diffraction, we observe photodoping of the low-spin lattice within ~150 femtoseconds. Above a ~16% photodoping threshold, the transition to the high-spin phase occurs following an incubation period assigned to vibrational energy redistribution within the nanorods activating the molecular spin switching. Above ~60% photodoping, the incubation period disappears, and the transition completes within ~50 picoseconds, preceded by the elastic nanorod expansion in response to the photodoping. These results support the feasibility of spin transition materials-based GHz optical switching applications.

Keywords

Spin transition materials, nanoscale, ultrafast dynamics, cooperativity, photo-switching, femtosecond X-ray techniques

Understanding what limits the speed and efficiency of photoinduced phase transitions is critical to the development of information technologies.[1-5] Photo-switchable spin transition (ST) molecular materials exhibit desired changes in optical, thermal, electrical and mechanical properties,[6, 7] but their integration in high frequency photo-switching applications is inhibited by slow and often inefficient transformations, associated with strain wave propagation and thermalization processes.[8] Reducing the size of ST molecular materials could therefore lead to faster and more efficient photo-switching, but experimental challenges have so far hindered a deeper understanding of the photo-switching mechanisms, associated timescales and rate-limiting processes at the nanoscale. The photo-switching process of ST microcrystals exhibits three steps that have not yet been conclusively resolved at the few nanometers scale: (1) Photon absorption at random lattice locations can result in light-induced excited spin state trapping (LIESST) that switches the molecular sites from a diamagnetic low-spin (LS) to a paramagnetic high-spin (HS) electronic configuration within ~150 femtoseconds.[9-11] (2) If the associated metal-ligand bond weakening and molecular swelling at the photoinduced HS sites triggers sufficiently strong intermolecular interactions, the spin conversion may be amplified during an 'elastic step' that is driven by material-scale volume expansion resulting from the stress-strain response to photodoping.[12-14] Elastic switching was observed in the nanosecond range for microcrystals, and this timescale has been associated with the ratio between system size and strain wave propagation velocity. [12, 14, 15] However, the roles of photoinduced thermal energy and strain for the switching dynamics have not been fully disentangled and recent work indicates that the ST does not occur simultaneously with the lattice expansion.[16, 17] While these studies suggest that downscaling to ~10 nm dimensions could shorten the elastic switching timescales to the picosecond regime, crucial for potential GHz photo-switching applications, this scaling law has not been validated on the few nanometer length scale.[17] (3) Bulk systems also show a slower third step in the LS-HS conversion on the nano- to millisecond timescales assigned to thermalization processes.[16, 18]

The design of highly cooperative Fe-triazole polymer-based ST nanorods has recently resolved a key challenge of the miniaturization process, as these compounds retain a ~40 K wide thermal hysteresis loop above room temperature for ~10 nm particles, close to the size limit at which cooperativity tends to disappear.[6] Complete photo-switching of Fe-triazole crystals was achieved using nanosecond excitation pulses, but the long duration of the photoexcitation process implied slow transformations characterized by lower material stresses.[19-21] The potential of femtosecond excitation pulses to achieve a sub-nanosecond, complete ST in Fe-triazole nanomaterials remained mostly unexplored.[18, 22, 23] Therefore, to investigate the photo-switching pathways and rate limiting processes of $[Fe(Htrz)_2(trz)](BF_4)$ nanorods with a length of 10-15 nm dispersed in solution (Figure 1a),[24] we have utilized femtosecond Fe $3p$-$1s$ (Kβ) X-ray emission spectroscopy (XES) and X-ray solution scattering (XSS) at the Linac Coherent Light Source (LCLS). XES is directly sensitive to the HS fraction $\gamma(t)$[10] while XSS independently monitors the time evolution of the nanocrystal lattice and excess energy dissipation during the photoinduced ST. The small nanorod size enables uniform photoexcitation and therefore allows differentiating between strain propagation and the ST. We continuously replenish the nanocrystals in a free-flowing liquid jet to avoid matrix effects[25] on the ST and photoinduced damage and build-up effects due to repeated nanorod irradiation, thus isolating the intrinsic nanomaterial response. With this approach, we

observe an ultrafast, nanoscale ST that is induced by a single femtosecond optical excitation pulse and completes within ~50 ps.

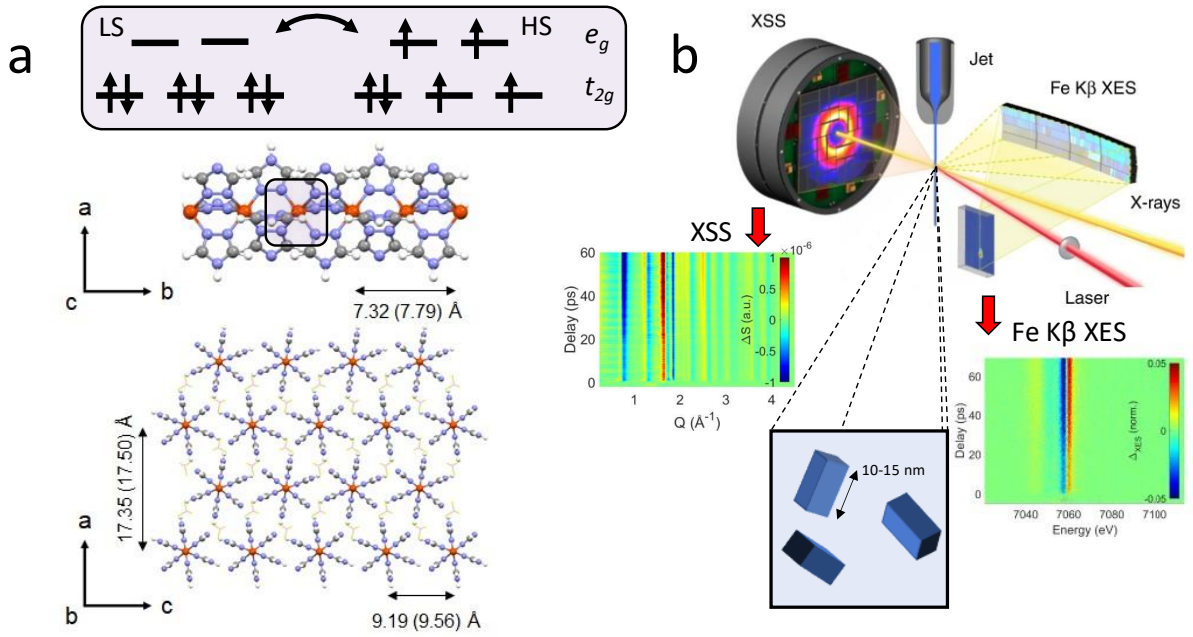

Figure 1: (a) Atomic structure of $[Fe(Htrz)_2(trz)](BF_4)$. Thermal equilibrium LS (HS) unit cell dimensions are indicated. Each Fe-center is hexacoordinated to nitrogen atoms of the triazole ligands, which link the Fe-sites together in one-dimensional chains along the crystallographic *b*-axis. The chains are stacked along the *a*- and *c*-axes with tetrafluoroborate counterions in between. Van der Waals and hydrogen bonding interactions define the three-dimensional nanorod structure.[26] The Fe(II) molecular centers switch between the LS and HS electronic configurations. In the LS configuration, the t_{2g}-subset (π-bonding) of the metal *d*-orbitals (O_h-symmetry) is fully occupied. In the HS configuration, two electrons are promoted from the t_{2g}-subset into the e_g-subset (σ-antibonding). (b) Scheme of the experimental setup at the XCS end station at the LCLS adapted from Kjaer *et al*.[9] with permission from the Royal Society of Chemistry. The shown time-dependent X-ray solution scattering and Fe Kβ XES difference maps were collected using an excitation fluence of 35 mJ/cm^2.

Results

X-ray emission spectroscopy: Fe Kβ main line XES predominantly fingerprints the spin and oxidation state at the core hole excited Fe-site via the 3*p*-3*d* exchange interaction, while being less sensitive to the chemical environment.[27-29] Therefore, the spin state of photoexcited molecular systems in solution can be tracked on the femtosecond timescale by fitting normalized time-dependent Kβ XES spectra with independently measured, appropriately chosen reference spectra.[10] We adopt this methodology to quantify the photo-induced time-dependent HS fraction $\gamma(t)$ for different excitation fluences (Figure 2). Starting from the LS phase, $\gamma(t)$ increases within ~150 fs (Figure 2c), a timescale commonly associated with LIESST in octahedral Fe-N compounds in both solution and crystals.[30] As shown later from the XSS analysis, this initial step in $\gamma(t)$ precedes the lattice response to photoexcitation, consistent with an intramolecular driving mechanism. LIESST involves successive intersystem crossing steps promoting two electrons from the π-bonding into the σ-antibonding subset of molecular orbitals (Figure 1a). This electronic structure change elongates the six Fe-N distances of each photoexcited $[Fe(Htrz)_2(trz)](BF_4)$ molecular unit by ~0.2 Å, and thus, the unit cell volume increases by ~11 %.[26, 31] LIESST therefore creates transient structural defects at random photoexcited locations in the LS lattice (photodoping), which correspond to small polarons that trigger lattice expansion. Following photodoping, $\gamma(t)$ increases more gradually within tens of picoseconds. For lower photodoping fractions, an incubation period (t_1) separates the molecular step due to LIESST from the less abrupt secondary LS-HS conversion step (Figure 2c). Towards higher photodoping fractions, t_1 shortens and $\gamma(t)$ approaches unity within tens of picoseconds, indicating nearly complete nanorod LS-HS phase conversion in the entire probed volume.

To quantify t_1, the photodoping fraction and magnitude of secondary spin conversion associated with the slower ST kinetics, we then fit $\gamma(t)$ for different fluences as described in Supplementary Note 1 (Figure 2c). The fitted photodoping fraction is approximately linear in the excitation fluence while the magnitude of secondary spin conversion saturates at higher excitation fluences due to nearly complete nanorod conversion. t_1 shortens from ~29 picoseconds to below 1 picosecond when the photodoping fraction increases from ~12% to ~70% (Supplementary Table 1). The fitted values represent averages of the ~50 μm liquid sample jet in which the photodoping fraction decays exponentially along the optical pump beam direction (Figure 2d). In the presence of a significant photodoping gradient, the observation of nearly complete LS-HS conversion at higher excitation fluences is indicative of a photodoping threshold γ_{th}, above which a nanorod transforms to the HS phase entirely. For lower photodoping fractions, the threshold γ_{th} therefore separates two spatial regions of switching and non-switching nanorods in the sample jet as depicted in Figure 2d. At the lowest fluence (10 mJ/cm^2), the fit indicates incomplete conversion (Figure 2c), and we use the associated photodoping fraction and secondary spin conversion magnitude to estimate the photodoping threshold as $\gamma_{th} = 0.16 \pm 0.01$ with the procedure described in Supplementary Note 1.

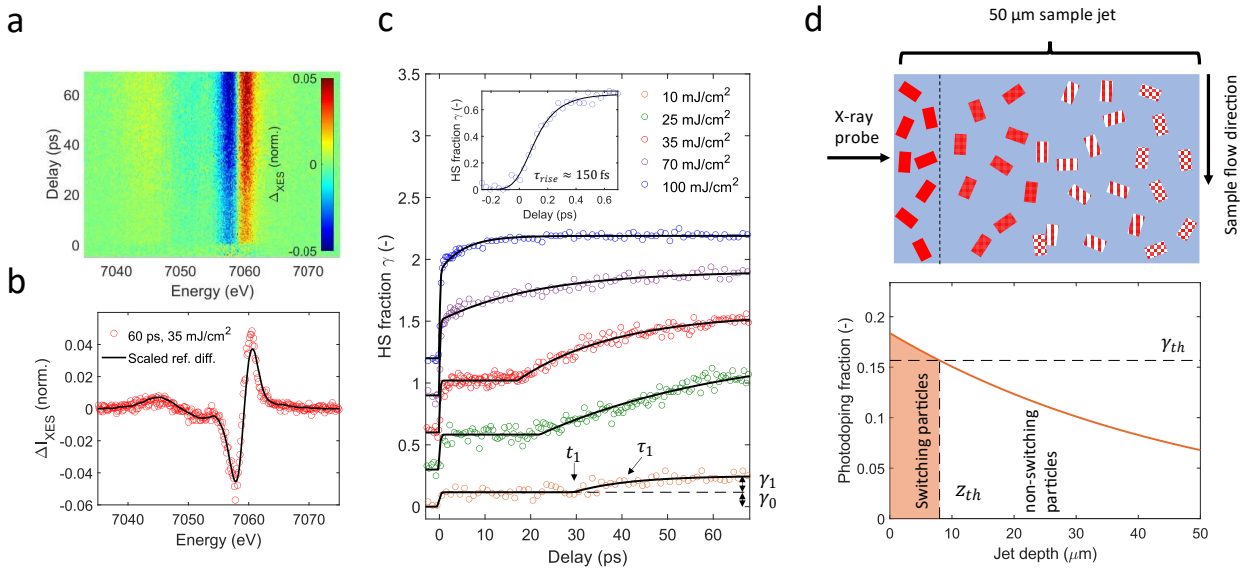

Figure 2: (a) X-ray emission difference signal of $[Fe(Htrz)_2(trz)](BF_4)$ as a function of X-ray emission energy and pump-probe delay for an excitation fluence of 35 mJ/cm^2. Details about the data reduction can be found in the Methods section. (b) Comparison of the normalized X-ray emission difference signal at 60 picoseconds with the scaled difference of quintet ($[Fe(phenanthroline)_2(NCS)_2]$) and singlet ($[Fe(2,2'\text{-bipyridine})_3]^{2+}$) reference spectra from Zhang *et al.*[10] (c) Extracted time evolution of the HS fraction for different excitation fluences including kinetic fits as described in the text with photodoping fraction γ_0 remaining constant up to t_1 when the HS fraction increases again by γ_1 within τ_1. The inset shows the time evolution of the HS fraction in the sub-picosecond range collected for an excitation fluence of 100 mJ/cm^2. (d) Illustration of the regions of switching and non-switching photoexcited nanorods as seen by the X-ray probe in the sample liquid jet. The photodoping fraction decreases exponentially through the jet and z_{th} denotes the jet depth separating the regions of switching and non-switching particles. γ_{th} is the photodoping threshold calculated from the data set collected with an excitation fluence of 10 mJ/cm^2.

X-ray solution scattering and diffraction: To correlate $\gamma(t)$ with the nanorod structural and thermal responses and therefore identify the origin of the observed photodoping threshold and incubation period t_1, we utilize the simultaneously collected XSS data in the momentum transfer range Q = 0.5 – 4.5 Å^{-1}, which is sensitive to intra- and interchain structural features.[31] The time-dependent differences between laser-excited and ground state total scattering curves (Figures 1b and 3a) exhibit distinct Bragg-reflection features encoding the photoinduced nanorod structural response. After a few hundred femtoseconds, the recorded differences resemble the difference of pure HS/LS phase powder X-ray diffraction curves measured at thermal equilibrium (395 K/298 K) (Figures 3a-b), indicating that the photoexcited nanorods exhibit significant increases in all three lattice parameters similar as in the thermal equilibrium HS structure (Figure 1a). The features observed in the time-dependent differences can be associated with groups of Bragg reflections of the *Pnma* HS and LS crystal structures[31] but time-dependent amplitude changes and peak shifts

result in deviations with respect to the scaled thermal equilibrium difference curve of the two phases (Supplementary Note 2). However, due to the large width of the diffraction features associated with the small nanorod size and the large number of diffraction peaks present within the limited Q-range of the measurement, we are unable to perform a quantitative refinement of the atomic positions. To analyze the nanocrystal structural evolution during the photoinduced phase transition, we consider different features that are separable along the momentum transfer axis and associated with the nanorod lateral and longitudinal (b-axis) directions, respectively. In the Q-ranges around ~0.75 Å^{-1} and ~1.28 Å^{-1}, we identify isolated features in the XSS difference maps that can be assigned to the (200)/(101) and (301)/(002) Bragg reflections, respectively (Figure 3b).[31] These features therefore reflect lateral structural changes. In contrast, the Q-range 1.70-1.95 Å^{-1} is also sensitive to changes along the polymer axis, predominantly via the (121)-reflection.[31] As described in Supplementary Note 2, we have therefore extracted the time evolution of the associated diffraction features for low and high photodoping conditions and compared them with $\gamma(t)$ determined from XES (Figures 3c-d). All peak positions were normalized to the respective differences between the thermal equilibrium LS/HS values. Both (200)/(101) and (301)/(002) peak positions show qualitatively similar behavior. The observed shifts towards lower Q indicate rapid lateral expansion towards a maximum value that is reached within ~1.5 picoseconds (Figures 3c-d). The peak positions then partially shift back towards the equilibrium value of the LS phase. Along the polymer axis, the lattice expansion occurs on a slower timescale as evidenced by the ~4 picoseconds initial partial shift of the (121)-reflection towards the HS equilibrium value. These findings are further supported by a Le Bail fit of the time-dependent X-ray scattering data as described in Supplementary Note 5. The time dependence of these peak features therefore indicates that the stress-strain response to the photodoping process initiates an overdamped nanorod breathing response.[32, 33] The observed decoupling of $\gamma(t)$ from the nanorod breathing mode dynamics shows the acoustic phonon response does not control the HS population (Figures 3c-d). The observed volume expansion is a displacive process, driven by the long-lived fraction of photoinduced HS centers of higher volume. For a nanorod with ~10-15 nm length and 5 – 7 nm width, the observed ~4 picosecond longitudinal expansion and ~1.5 picosecond lateral expansion timescales indicate a strain wave propagation velocity in the ~2.5 – 3.8 km/s range, within the reported range for ST compounds.[18] At later delays, all peak positions exhibit a time evolution similar to $\gamma(t)$, showing an incubation period that shortens towards higher photodoping fractions, followed by a gradual increase towards the HS phase equilibrium value. Importantly, for lower photodoping fractions, t_1 significantly exceeds the ~4 picosecond timescale of the initial lattice response to photodoping, which shows that the latter does not directly drive the ST. During the secondary HS conversion process within τ_1, the extracted lattice parameters indicate delayed expansion along the polymer axis compared to the orthogonal directions (Figures 3c-d and Supplementary Figure 14). The estimated low nanorod concentration (~ 1 μM) in ethanol used during the experiment indicates relatively large mean distances between nanorods. Therefore, the potential influence of solvent-mediated nanorod interactions on unit cell dimensions is not considered.

XSS also tracks the dissipation of thermal excess energy from the photoexcited nanorods into the solvent.[34] Using the procedure described in Supplementary Note 2, we therefore quantify the time-

dependent changes in the bulk solvent temperature and density, finding that within ~100 picoseconds, ~25% of the optically deposited excess energy transitions to the solvent, while ~75% remains within the nanorods. Inspection of the time-dependent Bragg peak intensities obtained from the Le Bail fit (Supplementary Note 5) indicates that the observed intensity changes are likely dominated by the intramolecular structure changes associated with the evolving HS fraction, which limits our ability to track the temperature evolution within the nanorods.

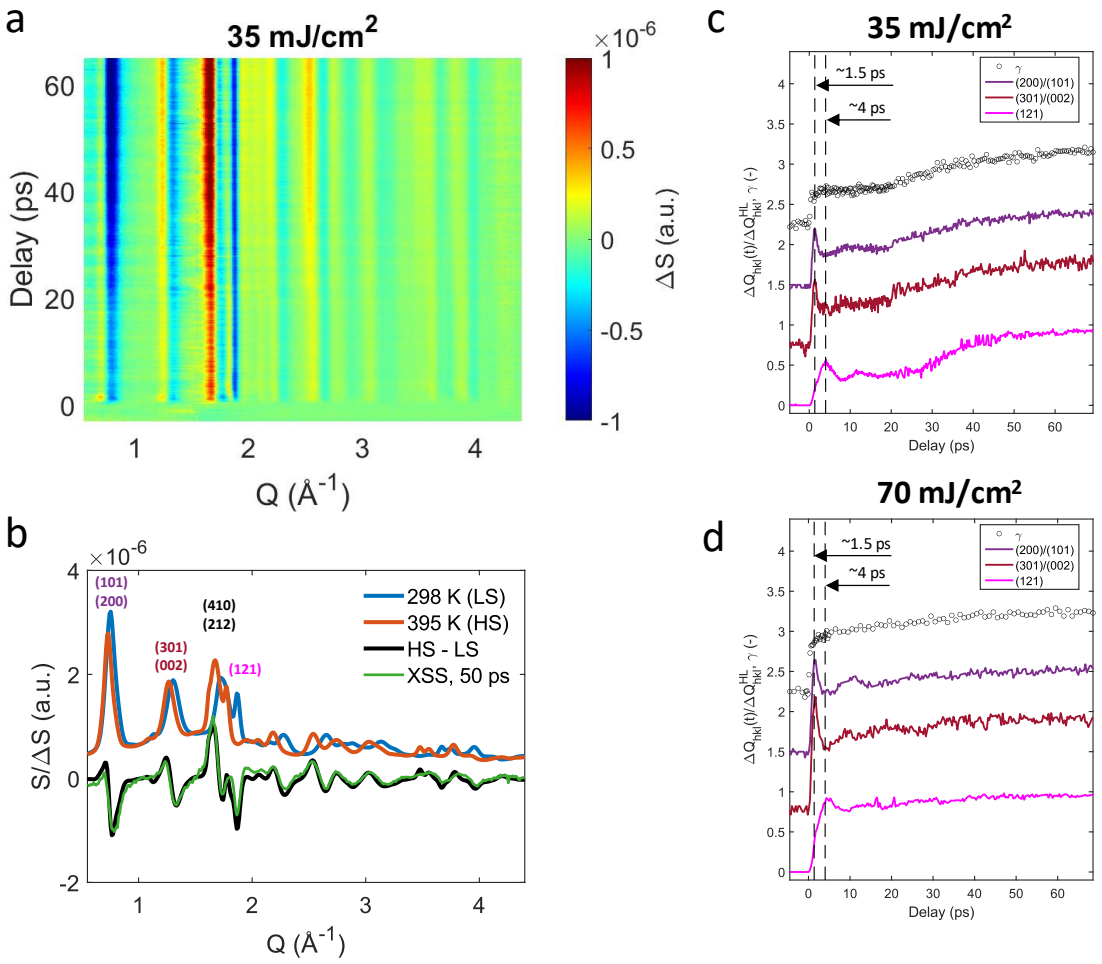

Figure 3: (a) Time-dependent XSS difference map of $[Fe(Htrz)_2(trz)](BF_4)$ measured using an excitation fluence of 35 mJ/cm^2. (b) Powder X-ray diffraction of $[Fe(Htrz)_2(trz)](BF_4)$ collected at 298 K (blue) and 395 K (red). (*hkl*) Miller indices of the strongest Bragg reflections are indicated. The difference of the curves collected at 395 K and 298 K is shown in black and compared with the transient difference curve at 50 ps (green) from the 35 mJ/cm^2 data set shown in (a). (c-d) Comparison of the HS fraction $\gamma(t)$ determined from XES with the relative position of different diffraction peaks $\Delta Q_{hkl}(t) = Q_{hkl}(t) - Q_{hkl}^{LS}$ normalized to the difference between the respective thermal equilibrium HS/LS values $\Delta Q_{hkl}^{HL} = Q_{hkl}^{HS} - Q_{hkl}^{LS}$. (c) shows data for an excitation fluence

of 35 mJ/cm^2 and (d) shows data for 70 mJ/cm^2. Vertical lines indicate expansion timescales along different directions of the nanorods.

Discussion

In a previous study focused on driving the ST at the material scale via rapid non-equilibrium lattice dynamics, Bertoni *et al*. photoexcited a weakly cooperative ST solid with femtosecond optical pulses.[12] For few hundred nano- to micrometer single crystals, they reported a LIESST process, followed by a gradual partial increase in $\gamma(t)$ that occurred on the nanosecond timescales, shortening towards smaller crystal sizes.[12] For microcrystals of the same material, Volte *et al*. reported a significant delay between the lattice expansion and the increase in $\gamma(t)$ assigned to the presence of molecular energy barriers between the LS and HS electronic configurations.[17] While the photodoping fraction remained well below 10%, this experiment pointed to a potential bottleneck limiting the achievable switching timescales at the nanoscale.

Here, we have combined femtosecond UV-excitation of ~10-15 nm strongly cooperative Fe-triazole nanorods with femtosecond XES and XSS probes to track $\gamma(t)$ and the lattice evolution separately. Using a free-flowing liquid jet enables high photodoping fractions without sample degradation. First, $\gamma(t)$ increases within ~150 femtoseconds due to LIESST, and the lattice accommodates the changes in molecular bonding within ~5 picoseconds, via an anisotropic structural response. Above a ~16% photodoping threshold, we observe a complete ST. Below ~60% photodoping, the ST proceeds after an incubation period spanning tens of picoseconds, which unambiguously demonstrates that it is not directly driven by the ~5 picosecond elastic expansion of the nanorod (Figure 3c), consistent with Volte *et al*.[17]

In the following, we therefore discuss the implications of significant amounts of photoinduced strain and thermal energies within the nanorods for the achievable ST timescales. The role of volume strain in cooperative and hysteretic ST materials was recently discussed within the Landau theory of phase transitions,[35, 36] through a Taylor expansion of the Gibbs potential in the ST order parameter $q = 2\gamma - 1$ (Supplementary Note 4):

$$G(T, q) = a(T_{ST} - T)q + \frac{1}{2}Bq^2 + \frac{1}{4}Cq^4$$

The ST temperature T_{ST} and the coefficient B include the effects of volume strain through the elastic energy and its elastic coupling with q. Strong elastic interactions result in $B < 0$, which reproduces the first-order and hysteretic ST curve of the compound. As shown in the bottom-left panel in Figure 4, at room temperature, well below T_{ST}, only the LS state ($\gamma \simeq 0$) is stable, while the LS and HS states are bistable within the hysteresis region, as shown at $T = T_{ST} = 360\ K$. In the following, we show that this formalism captures key features of the observed ultrafast photoinduced ST.

Photodoping is homogeneous within the nanorods and therefore the resulting volume expansion (dv_s) equilibrates rapidly within ≃5 ps, modifying the Gibbs potential on this timescale. dv_s renormalizes T_{ST} and stabilizes the HS state at lower temperature (Supplementary Note 4). This effect can be quantified from equilibrium studies on Zn-doped samples because the inactive Zn(II) ions exhibit a similar ionic radius to that of the HS Fe(II) ions.[37, 38] Experiments by Lefter *et al*. on $[Fe_{1-x}Zn_x(Htrz)_2(trz)](BF_4)$ show that increasing the Zn-doping fraction decreases the transition

temperature almost linearly.[39] From the reported downshift from ~385 K to ~320 K for a ~43% Zn-doping fraction, we therefore estimate a downshift to ~361 K, well above room temperature, for a ~16% Zn-doping fraction. The energy of the absorbed photons of the LIESST process (~4.66 eV) exceeds the HS-LS energy gap (~0.3 eV),[40] which results in the deposition of significant amounts of vibrational energy that is redistributed within the nanorods through coupling between intra- and intermolecular vibrations. While our measurement is not directly sensitive to these processes, they typically occur on the few to tens of picosecond timescales,[17, 41, 42] comparable with the incubation periods t_1 observed in the XES data (Supplementary Table 1). Furthermore, common heat capacities of ST materials[43, 44] suggest that at the ~16% switching threshold, complete equilibration of the photoinduced vibrational excess energy would raise the nanorod temperature close to the downshifted transition temperature of the photodoped material (Supplementary Note 2), thus enabling the ST.[24]

For the ~16-60% photodoping range, the Gibbs potential exhibits destabilized LS ($\gamma < 0.5$) and stabilized HS ($\gamma > 0.5$) states due to photoinduced volume strain, but the energy barrier hinders direct relaxation towards the equilibrium HS state (Figure 4, middle-left panel). Vibrational energy redistribution then drives the nanorods towards thermal equilibrium at higher temperatures, lowering the energy barrier during this thermoelastic step.[15] The incubation period is not associated with any change in the unit cell dimensions. Therefore, it likely arises from the presence of the energy barrier and reflects the time required to redistribute energy into the vibrational motions promoting the spin conversion at residual LS sites. The observed delayed volume expansion during both the initial LIESST and secondary LS-HS conversion processes (Supplementary Note 5, Supplementary Figure 14) then shows that the metal-ligand intramolecular bond expansion associated with the spin state change primarily triggers a photoinduced lattice strain, equilibrating more rapidly along lateral dimensions compared to the longitudinal direction. Higher photodoping increases both vibrational energy and strain. The strain-modified Gibbs potential then shows a stronger LS destabilization and lower energy barrier towards HS conversion, consistent with the observed shortening of t_1. For sufficiently high photodoping fractions, the energy barrier vanishes, and the system relaxes directly towards the HS state (Figure 4, upper-left panel). From the Zn-doping studies by Lefter *et al*.[39] we extrapolate that a ~60% Zn-doping fraction would downshift the transition temperature to room temperature. Therefore, t_1 should disappear, and the ST should be enabled by the photoinduced lattice expansion. This agrees with our measurements, as for photodoping fractions above ~60%, the ST occurs without a resolvable incubation period and completes within ~50 ps (Figure 2c and Supplementary Table 1).

These considerations rationalize the observed shortening and disappearance of the incubation period towards higher photodoping fractions, but do not explain the observed LS-HS conversion rates (τ_1) in the absence of a mechanoelastic barrier at photodoping fractions above ~60%. Even for the highest photodoping fractions, the secondary increase in $\gamma(t)$ occurs within tens of picoseconds and therefore lags the ~5 picosecond nanorod volume expansion (Figure 3d). Furthermore, $\gamma(t)$ does not exhibit the overdamped breathing response observed for the nanorod lateral and longitudinal lattice spacings, which demonstrates the decoupling of the ST from the acoustic response and the limitations of size reduction on the ST rate at the ~10 nm scale. The decoupling of $\gamma(t)$ from the observed unit cell size shows that the spin state conversion rates at

the individual Fe sites must involve an activated reorganization of intra-cell structural degrees of freedom, such as Fe-ligand bond length and bond angle changes. These findings indicate that a more complete understanding of the Gibbs potential that controls the ultrafast photoinduced ST process in Fe-triazole nanorods must capture the influence of photodoping and temperature on both inter- and intra-unit cell interactions. This feedback dynamically modifies the thermodynamic potential as spin conversion occurs, as shown in Figure 4.

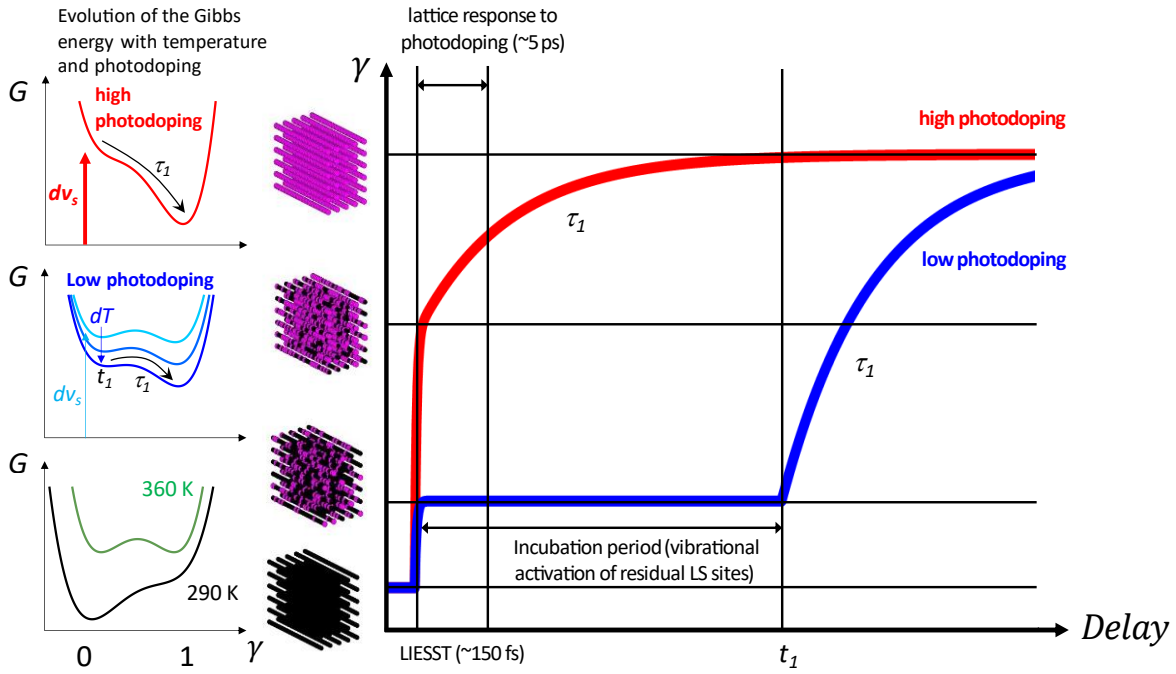

Figure 4: Proposed scheme for the photoinduced spin transition of $[Fe(Htrz)_2(trz)](BF_4)$ nanorods. The lower-left panel shows the Gibbs potentials at temperatures below (black) and within (green) the thermal hysteresis region. LIESST modifies the Gibbs potential via photoinduced volume strain dv_s and a temperature increase dT, both destabilizing the LS state and stabilizing the HS state. For low photodoping (middle-left panel), dv_s remains small and an energy barrier towards HS formation prevents prompt spin conversion. Vibrational energy equilibration then leads to an increase in the nanorod temperature by dT. The spin transition occurs on a timescale τ_1 after an incubation period t_1 that reflects activation of the residual LS sites. At high photodoping fractions (upper-left panel), dv_s becomes sufficiently large and cooperative interactions drive the nanorods into the HS phase prior to significant thermal activation. The time evolution of the HS fraction γ under low (blue) and high (red) photodoping conditions is visualized on the right side.

Conclusions

ST polymers have emerged as viable candidates for miniaturization and device integration of cooperative ST systems, capable of retaining thermal hysteresis at the few nanometer nanorods.[45] [6, 24] However, the switching mechanisms, timescales and efficiencies of ST nanomaterials remain poorly understood. Using a combination of femtosecond X-ray techniques to study ~10-15 nm long Fe-triazole nanorods, we observe a ~150 femtosecond photodoping process, followed by a complete ST occurring above a ~16% photodoping threshold. Below ~60% photodoping, the occurrence of the nanorod ST requires both mechanical destabilization of the LS lattice and excess vibrational energy redistribution during an incubation period prior to a secondary completion of the ST. When the photodoping fraction increases, higher amounts of vibrational excess energy are deposited within the nanorods, and the stronger lattice expansion favors HS conversion. Both effects shorten the incubation period that determines the onset of the ST. Above ~60% photodoping, the ST completes within ~50 picoseconds without an incubation period. Critically, the ST mechanism decouples from the observed lattice degrees of freedom on these ultrafast timescales, which indicates an upper bound for the ST switching rate that can be achieved through size reduction. Nevertheless, in these highly cooperative nanocrystals under high photodoping conditions, the observed ST proceeds two orders of magnitude faster than previously reported for ST compounds,[17] which could promote developments towards ST materials-based photo-switching devices operating at GHz repetition rates.

Methods

Fe-triazole ($[Fe(Htrz)_2(trz)]BF_4$) nanorods were synthesized and characterized as described in Supplementary Note 3. For the time-resolved X-ray experiments, they were suspended in ethanol at 10-15 mM Fe concentrations. Nanorod dimensions were estimated as ~7 x 13 x 5 nm^3 based on transmission electron microscopy and powder X-ray diffraction linewidth analysis (Supplementary Note 1).

Temperature dependent steady state powder X-ray diffraction data were collected at beamline 11-ID-B at the Advanced Photon Source (APS) using 58.68 keV (0.2113 Å) X-rays. Dried Fe-triazole powder samples were mounted in a capillary at a detector-to-sample distance of 95 cm and measured at room temperature and 395 K. X-rays were detected using a Perkin Elmer XRD1621 amporphous silicon detector and the temperature was adjusted using an Oxford cryosystems cryostream 700 plus.

The Kβ XES and XSS data were simultaneously collected at the X-ray Correlation Spectroscopy (XCS) instrument[46] at the Linac Coherent Light Source (LCLS). We used an HPLC pump combined with a ~50 μm inner diameter cylindrical capillary to form a liquid jet and continuously recirculate the sample. Optical excitation was performed nearly collinearly to the incident X-rays with 50 fs FWHM, 266 nm laser pulses generated by frequency-tripling the 800 nm output of a Ti:sapphire regenerative amplifier laser system (Coherent, Legend). Data were collected at various pump laser fluences in the range ~10-100 mJ/cm^2. The sample was probed by 9.6 keV self-amplified stimulated emission (SASE) X-ray pulses (~10^{12} photons/pulse, 120 Hz, 50 fs) shortly after exiting the capillary in the region of laminar flow. The time delay between the laser and X-ray pulse was determined via the timing tool[47] installed at XCS. Using Be compound refractive lenses, the X-ray pulses were focused to a 50 μm diameter spot size on the sample jet. A high-energy resolution X-ray emission spectrometer, based on the von Hamos geometry, was used to capture the Fe Kβ XES signal.[48] The spectrometer was equipped with 4 cylindrically bent (0.5 m radius) Ge(620) crystal analyzers and set to cover the Bragg angle range from 78.1° to 80.5° corresponding to an energy range of 7.027 to 7.083 keV. The Kβ XES data were collected using an ePix100 detector.[49] To detect the XSS data, a 2.3M CSPAD was used in forward scattering geometry.[49] Full 2D images of the XES and XSS detectors were read out shot-to-shot and subsequently processed and binned according to their pump-probe delay. XES spectra were extracted by integrating the intensity in a rectangular area of interest containing a few pixels along the non-dispersive axis. The emission energy was calibrated by matching the laser off spectrum to a singlet reference spectrum ($[Fe(2,2'\text{-bipyridine})_3]^{2+}$) from Zhang *et al*.[10] All XES spectra were normalized to the total Kβ main line area. The time-dependent difference spectra shown in Figures 1b, 2a-b, and Supplementary Figure 1 are then calculated by subtracting the laser off spectrum at each time delay. XSS data reduction and analysis procedures are described in van Driel *et al.*[50]

Acknowledgements

A.A.C, K.K., E.B., and K.J.G. acknowledge support from the U.S. Department of Energy, Office of Science, Basic Energy Sciences, Chemical Sciences, Geosciences, and Biosciences Division. Use of the Linac Coherent Light Source (LCLS), SLAC National Accelerator Laboratory, was supported by the U.S. Department of Energy, Office of Science, Office of Basic Energy Sciences under Contract No. DE-AC02-76SF00515. This research used resources of the Advanced Photon Source, a U.S. Department of Energy (DOE) Office of Science user facility operated for the DOE Office of Science by Argonne National Laboratory under Contract No. DE-AC02-06CH11357.

Part of this work was performed at the Stanford Nano Shared Facilities (SNSF), supported by the National Science Foundation under award ECCS-2026822.

M.R. acknowledges support via an Early Postdoc.Mobility fellowship from the Swiss National Science Foundation (Project number P2ELP2_158890).

Author contributions

M.R. and K.J.G. designed the research and experiments. M.R., K.K., K.L., E.B., D.B.Z., R.A.M., T.v.D., S.N., M.K., D.S. and A.A.C. conducted the experiment at the LCLS. M.R., K.K., K.L., E.B., D.B.Z. and A.A.C. analyzed the data. M.R. and D.B.Z. synthesized the sample. E.C., M.L. and M.C. proposed the volume strain discussion. O.B. conducted the XRD experiment at the APS. M.R. A.A.C. and K.J.G. wrote the manuscript with input from all the authors.

Competing interests

The authors declare no competing interests.

Data and code availability

All relevant data and analysis scripts used in this study are available from the corresponding authors upon reasonable request.

Supplementary Information

- Supplementary Note 1: X-ray emission data analysis
- Supplementary Note 2: X-ray solution scattering data analysis
- Supplementary Note 3: Nanoparticle synthesis and characterization
- Supplementary Note 4: Landau model and volume strain

- Supplementary Note 5: Extraction of unit cell dimensions from the excited state scattering curves

References

1. Nasu, K., *Photoinduced Phase Transitions*. World Scientific Publishing Co. Pte. Ltd.: Singapore, 2004.
2. Tao, Z.; Zhou, F.; Han, T.-R. T.; Torres, D.; Wang, T.; Sepulveda, N.; Chang, K.; Young, M.; Lunt, R. R.; Ruan, C.-Y., The nature of photoinduced phase transition and metastable states in vanadium dioxide. *Scientific Reports* **2016,** *6*, 38514.
3. Beaud, P.; Caviezel, A.; Mariager, S. O.; Rettig, L.; Ingold, G.; Dornes, C.; Huang, S. W.; Johnson, J. A.; Radovic, M.; Huber, T.; Kubacka, T.; Ferrer, A.; Lemke, H. T.; Chollet, M.; Zhu, D.; Glownia, J. M.; Sikorski, M.; Robert, A.; Wadati, H.; Nakamura, M.; Kawasaki, M.; Tokura, Y.; Johnson, S. L.; Staub, U., A time-dependent order parameter for ultrafast photoinduced phase transitions. *Nature Materials* **2014,** *13*, 923.
4. Ichikawa, H.; Nozawa, S.; Sato, T.; Tomita, A.; Ichiyanagi, K.; Chollet, M.; Guerin, L.; Dean, N.; Cavalleri, A.; Adachi, S.-i.; Arima, T.-h.; Sawa, H.; Ogimoto, Y.; Nakamura, M.; Tamaki, R.; Miyano, K.; Koshihara, S.-y., Transient photoinduced 'hidden' phase in a manganite. *Nature Materials* **2011,** *10*, 101.
5. Zong, A.; Kogar, A.; Bie, Y.-Q.; Rohwer, T.; Lee, C.; Baldini, E.; Ergeçen, E.; Yilmaz, M. B.; Freelon, B.; Sie, E. J.; Zhou, H.; Straquadine, J.; Walmsley, P.; Dolgirev, P. E.; Rozhkov, A. V.; Fisher, I. R.; Jarillo-Herrero, P.; Fine, B. V.; Gedik, N., Evidence for topological defects in a photoinduced phase transition. *Nature Physics* **2019,** *15* (1), 27-31.
6. Kahn, O.; Martinez, C. J., Spin-Transition Polymers: From Molecular Materials Toward Memory Devices. *Science* **1998,** *279* (5347), 44-48.
7. Létard, J.-F.; Guionneau, P.; Goux-Capes, L., Towards Spin Crossover Applications. In *Spin Crossover in Transition Metal Compounds III*, Gütlich, P.; Goodwin, H. A., Eds. Springer Berlin Heidelberg: Berlin, Heidelberg, 2004; pp 221-249.
8. Ridier, K.; Molnár, G.; Salmon, L.; Nicolazzi, W.; Bousseksou, A., Hysteresis, nucleation and growth phenomena in spin-crossover solids. *Solid State Sciences* **2017,** *74*, A1-A22.
9. Kjær, K. S.; Van Driel, T. B.; Harlang, T. C. B.; Kunnus, K.; Biasin, E.; Ledbetter, K.; Hartsock, R. W.; Reinhard, M. E.; Koroidov, S.; Li, L.; Laursen, M. G.; Hansen, F. B.; Vester, P.; Christensen, M.; Haldrup, K.; Nielsen, M. M.; Dohn, A. O.; Pápai, M. I.; Møller, K. B.; Chabera, P.; Liu, Y.; Tatsuno, H.; Timm, C.; Jarenmark, M.; Uhlig, J.; Sundstöm, V.; Wärnmark, K.; Persson, P.; Németh, Z.; Szemes, D. S.; Bajnóczi, É.; Vankó, G.; Alonso-Mori, R.; Glownia, J. M.; Nelson, S.; Sikorski, M.; Sokaras, D.; Canton, S. E.; Lemke, H. T.; Gaffney, K. J., Finding intersections between electronic excited state potential energy surfaces with simultaneous ultrafast X-ray scattering and spectroscopy. *Chemical Science* **2019,** *10* (22), 5749-5760.
10. Zhang, W.; Alonso-Mori, R.; Bergmann, U.; Bressler, C.; Chollet, M.; Galler, A.; Gawelda, W.; Hadt, R. G.; Hartsock, R. W.; Kroll, T.; Kjaer, K. S.; Kubicek, K.; Lemke, H. T.; Liang, H. W.; Meyer, D. A.; Nielsen, M. M.; Purser, C.; Robinson, J. S.; Solomon, E. I.; Sun, Z.; Sokaras, D.; van Driel, T. B.; Vanko, G.; Weng, T.-C.; Zhu, D.; Gaffney, K. J., Tracking excited-state charge and spin dynamics in iron coordination complexes. *Nature* **2014,** *509* (7500), 345-348.
11. Bressler, C.; Milne, C.; Pham, V.-T.; ElNahhas, A.; van der Veen, R. M.; Gawelda, W.; Johnson, S.; Beaud, P.; Grolimund, D.; Kaiser, M.; Borca, C. N.; Ingold, G.; Abela, R.; Chergui, M., Femtosecond XANES Study of the Light-Induced Spin Crossover Dynamics in an Iron(II) Complex. *Science* **2009,** *323* (5913), 489-492.
12. Bertoni, R.; Lorenc, M.; Cailleau, H.; Tissot, A.; Laisney, J.; Boillot, M.-L.; Stoleriu, L.; Stancu, A.; Enachescu, C.; Collet, E., Elastically driven cooperative response of a molecular material impacted by a laser pulse. *Nat Mater* **2016,** *15* (6), 606-610.
13. Collet, E.; Guionneau, P., Structural analysis of spin-crossover materials: From molecules to materials. *Comptes Rendus Chimie* **2018,** *21* (12), 1133-1151.

14. Lorenc, M.; Hébert, J.; Moisan, N.; Trzop, E.; Servol, M.; Buron-Le Cointe, M.; Cailleau, H.; Boillot, M. L.; Pontecorvo, E.; Wulff, M.; Koshihara, S.; Collet, E., Successive Dynamical Steps of Photoinduced Switching of a Molecular Fe(III) Spin-Crossover Material by Time-Resolved X-Ray Diffraction. *Physical Review Letters* **2009,** *103* (2), 028301.
15. Stoleriu, L.; Nishino, M.; Miyashita, S.; Stancu, A.; Bertoni, R.; Collet, E.; Lorenc, M.; Enachescu, C., Multiscale out-of-equilibrium dynamics driven by pulsed laser excitation in spin-crossover materials: A combined thermoelastic and mechanoelastic study. *Physical Review B* **2023,** *108* (1), 014306.
16. Bertoni, R.; Collet, E.; Cailleau, H.; Boillot, M.-L.; Tissot, A.; Laisney, J.; Enachescu, C.; Lorenc, M., Temperature dependence of the cooperative out-of-equilibrium elastic switching in a spin-crossover material. *Physical Chemistry Chemical Physics* **2019,** *21* (12), 6606-6612.
17. Volte, A.; Mariette, C.; Bertoni, R.; Cammarata, M.; Dong, X.; Trzop, E.; Cailleau, H.; Collet, E.; Levantino, M.; Wulff, M.; Kubicki, J.; Yang, F.-L.; Boillot, M.-L.; Corraze, B.; Stoleriu, L.; Enachescu, C.; Lorenc, M., Dynamical limits for the molecular switching in a photoexcited material revealed by X-ray diffraction. *Communications Physics* **2022,** *5* (1), 168.
18. Ridier, K.; Bas, A.-C.; Shalabaeva, V.; Nicolazzi, W.; Salmon, L.; Molnár, G.; Bousseksou, A.; Lorenc, M.; Bertoni, R.; Collet, E.; Cailleau, H., Finite Size Effects on the Switching Dynamics of Spin-Crossover Thin Films Photoexcited by a Femtosecond Laser Pulse. *Advanced Materials* **2019,** *31* (25), 1901361.
19. Galle, G.; Degert, J.; Mauriac, C.; Etrillard, C.; Letard, J. F.; Freysz, E., Nanosecond study of spin state transition induced by a single nanosecond laser shot on [Fe(NH2trz)3] compounds inside and outside their thermal hysteresis loops. *Chemical Physics Letters* **2010,** *500* (1), 18-22.
20. Gallé, G.; Deldicque, D.; Degert, J.; Forestier, T.; Létard, J.-F.; Freysz, E., Room temperature study of the optical switching of a spin crossover compound inside its thermal hysteresis loop. *Applied Physics Letters* **2010,** *96* (4), 041907.
21. Fouché, O.; Degert, J.; Jonusauskas, G.; Daro, N.; Létard, J.-F.; Freysz, E., Mechanism for optical switching of the spin crossover [Fe(NH2-trz)3](Br)2·3H2O compound at room temperature. *Physical Chemistry Chemical Physics* **2010,** *12* (12), 3044-3052.
22. Molnár, G.; Rat, S.; Salmon, L.; Nicolazzi, W.; Bousseksou, A., Spin Crossover Nanomaterials: From Fundamental Concepts to Devices. *Advanced Materials* **2018,** *30* (5), 1703862.
23. Nicolazzi, W.; Bousseksou, A., Thermodynamical aspects of the spin crossover phenomenon. *Comptes Rendus Chimie* **2018,** *21* (12), 1060-1074.
24. Coronado, E.; Galán-Mascarós, J. R.; Monrabal-Capilla, M.; García-Martínez, J.; Pardo-Ibáñez, P., Bistable Spin-Crossover Nanoparticles Showing Magnetic Thermal Hysteresis near Room Temperature. *Advanced Materials* **2007,** *19* (10), 1359-1361.
25. Bousseksou, A.; Molnár, G.; Salmon, L.; Nicolazzi, W., Molecular spin crossover phenomenon: recent achievements and prospects. *Chemical Society Reviews* **2011,** *40* (6), 3313-3335.
26. Urakawa, A.; Van Beek, W.; Monrabal-Capilla, M.; Galán-Mascarós, J. R.; Palin, L.; Milanesio, M., Combined, Modulation Enhanced X-ray Powder Diffraction and Raman Spectroscopic Study of Structural Transitions in the Spin Crossover Material [Fe(Htrz)2(trz)](BF4). *The Journal of Physical Chemistry C* **2011,** *115* (4), 1323-1329.
27. Pollock, C. J.; Delgado-Jaime, M. U.; Atanasov, M.; Neese, F.; DeBeer, S., Kβ Mainline X-ray Emission Spectroscopy as an Experimental Probe of Metal–Ligand Covalency. *Journal of the American Chemical Society* **2014,** *136* (26), 9453-9463.
28. Glatzel, P.; Bergmann, U., High resolution 1s core hole X-ray spectroscopy in 3d transition metal complexes—electronic and structural information. *Coordination Chemistry Reviews* **2005,** *249* (1), 65-95.

29. Vankó, G.; Neisius, T.; Molnár, G.; Renz, F.; Kárpáti, S.; Shukla, A.; de Groot, F. M. F., Probing the 3d Spin Momentum with X-ray Emission Spectroscopy: The Case of Molecular-Spin Transitions. *The Journal of Physical Chemistry B* **2006,** *110* (24), 11647-11653.
30. Field, R.; Liu, L. C.; Gawelda, W.; Lu, C.; Miller, R. J. D., Spectral Signatures of Ultrafast Spin Crossover in Single Crystal [FeII(bpy)3](PF6)2. *Chemistry – A European Journal* **2016,** *22* (15), 5118-5122.
31. Grosjean, A.; Négrier, P.; Bordet, P.; Etrillard, C.; Mondieig, D.; Pechev, S.; Lebraud, E.; Létard, J.-F.; Guionneau, P., Crystal Structures and Spin Crossover in the Polymeric Material [Fe(Htrz)2(trz)](BF4) Including Coherent-Domain Size Reduction Effects. *European Journal of Inorganic Chemistry* **2013,** *2013* (5-6), 796-802.
32. Szilagyi, E.; Wittenberg, J. S.; Miller, T. A.; Lutker, K.; Quirin, F.; Lemke, H.; Zhu, D.; Chollet, M.; Robinson, J.; Wen, H.; Sokolowski-Tinten, K.; Lindenberg, A. M., Visualization of nanocrystal breathing modes at extreme strains. *Nature Communications* **2015,** *6*, 6577.
33. Reid, A. H.; Shen, X.; Maldonado, P.; Chase, T.; Jal, E.; Granitzka, P. W.; Carva, K.; Li, R. K.; Li, J.; Wu, L.; Vecchione, T.; Liu, T.; Chen, Z.; Higley, D. J.; Hartmann, N.; Coffee, R.; Wu, J.; Dakovski, G. L.; Schlotter, W. F.; Ohldag, H.; Takahashi, Y. K.; Mehta, V.; Hellwig, O.; Fry, A.; Zhu, Y.; Cao, J.; Fullerton, E. E.; Stöhr, J.; Oppeneer, P. M.; Wang, X. J.; Dürr, H. A., Beyond a phenomenological description of magnetostriction. *Nature Communications* **2018,** *9* (1), 388.
34. Haldrup, K.; Christensen, M.; Meedom Nielsen, M., Analysis of time-resolved X-ray scattering data from solution-state systems. *Acta Crystallographica Section A* **2010,** *66* (2), 261-269.
35. Collet, E.; Azzolina, G., Coupling and decoupling of spin crossover and ferroelastic distortion: Unsymmetric hysteresis loop, phase diagram, and sequence of phases. *Physical Review Materials* **2021,** *5* (4), 044401.
36. Azzolina, G.; Bertoni, R.; Collet, E., General Landau theory of non-symmetry-breaking and symmetry-breaking spin transition materials. *Journal of Applied Physics* **2021,** *129* (8).
37. Revised effective ionic radii and systematic studies of interatomie distances in halides and chaleogenides. *Acta Cryst. A* **1976,** *32* (5), 751-767.
38. Sylla, M. S.; Baldé, C.; Daro, N.; Desplanches, C.; Marchivie, M.; Chastanet, G., On the Effect of the Internal Pressure on the Photoinduced Spin-Crossover Behavior of [FexM1–x(1,10-phenanthroline)2(NCS)2] Solid Solutions (M = NiII, ZnII, and CdII). *European Journal of Inorganic Chemistry* **2018,** *2018* (3-4), 297-304.
39. Lefter, C.; Tricard, S.; Peng, H.; Molnár, G.; Salmon, L.; Demont, P.; Rotaru, A.; Bousseksou, A., Metal Substitution Effects on the Charge Transport and Spin Crossover Properties of [Fe1–xZnx(Htrz)2(trz)](BF4) (trz = Triazole). *The Journal of Physical Chemistry C* **2015,** *119* (16), 8522-8529.
40. Kroeber, J.; Audiere, J.-P.; Claude, R.; Codjovi, E.; Kahn, O.; Haasnoot, J. G.; Groliere, F.; Jay, C.; Bousseksou, A., Spin Transitions and Thermal Hysteresis in the Molecular-Based Materials [Fe(Htrz)2(trz)](BF4) and [Fe(Htrz)3](BF4)2.cntdot.H2O (Htrz = 1,2,4-4H-triazole; trz = 1,2,4-triazolato). *Chemistry of Materials* **1994,** *6* (8), 1404-1412.
41. Kurnosov, A. A.; Rubtsov, I. V.; Burin, A. L., Communication: Fast transport and relaxation of vibrational energy in polymer chains. *The Journal of Chemical Physics* **2015,** *142* (1), 011101.
42. Marino, A.; Cammarata, M.; Matar, S. F.; Létard, J.-F.; Chastanet, G.; Chollet, M.; Glownia, J. M.; Lemke, H. T.; Collet, E., Activation of coherent lattice phonon following ultrafast molecular spin-state photo-switching: A molecule-to-lattice energy transfer. *Structural Dynamics* **2016,** *3* (2), 023605.
43. Roubeau, O.; Castro, M.; Burriel, R.; Haasnoot, J. G.; Reedijk, J., Calorimetric Investigation of Triazole-Bridged Fe(II) Spin-Crossover One-Dimensional Materials: Measuring the Cooperativity. *The Journal of Physical Chemistry B* **2011,** *115* (12), 3003-3012.
44. Sorai, M., Heat Capacity Studies of Spin Crossover Systems. In *Spin Crossover in Transition Metal Compounds III*, Gütlich, P.; Goodwin, H. A., Eds. Springer Berlin Heidelberg: Berlin, Heidelberg, 2004; pp 153-170.

45. Linares, J.; Codjovi, E.; Garcia, Y., Pressure and Temperature Spin Crossover Sensors with Optical Detection. *Sensors* **2012,** *12* (4), 4479-4492.
46. Alonso-Mori, R.; Caronna, C.; Chollet, M.; Curtis, R.; Damiani, D. S.; Defever, J.; Feng, Y.; Flath, D. L.; Glownia, J. M.; Lee, S.; Lemke, H. T.; Nelson, S.; Bong, E.; Sikorski, M.; Song, S.; Srinivasan, V.; Stefanescu, D.; Zhu, D.; Robert, A., The X-ray Correlation Spectroscopy instrument at the Linac Coherent Light Source. *Journal of synchrotron radiation* **2015,** *22* (3), 508-513.
47. Harmand, M.; Coffee, R.; Bionta, M. R.; Chollet, M.; French, D.; Zhu, D.; Fritz, D. M.; Lemke, H. T.; Medvedev, N.; Ziaja, B.; Toleikis, S.; Cammarata, M., Achieving few-femtosecond time-sorting at hard X-ray free-electron lasers. *Nature Photonics* **2013,** *7*, 215.
48. Alonso-Mori, R.; Kern, J.; Sokaras, D.; Weng, T.-C.; Nordlund, D.; Tran, R.; Montanez, P.; Delor, J.; Yachandra, V. K.; Yano, J.; Bergmann, U., A multi-crystal wavelength dispersive x-ray spectrometer. *Review of Scientific Instruments* **2012,** *83* (7), 073114.
49. Blaj, G.; Caragiulo, P.; Carini, G.; Carron, S.; Dragone, A.; Freytag, D.; Haller, G.; Hart, P.; Hasi, J.; Herbst, R.; Herrmann, S.; Kenney, C.; Markovic, B.; Nishimura, K.; Osier, S.; Pines, J.; Reese, B.; Segal, J.; Tomada, A.; Weaver, M., X-ray detectors at the Linac Coherent Light Source. *Journal of Synchrotron Radiation* **2015,** *22* (3), 577-583.
50. van Driel, T. B.; Kjær, K. S.; Biasin, E.; Haldrup, K.; Lemke, H. T.; Nielsen, M. M., Disentangling detector data in XFEL studies of temporally resolved solution state chemistry. *Faraday Discussions* **2015,** *177* (0), 443-465.